Proc. Natl. Acad. Sci. USA
Vol. 96, pp. 10134–10139, August 1999
Biophysics

Rotational symmetry of the C ring and a mechanism for the flagellar rotary motor

DENNIS R. THOMAS*, DAVID GENE MORGAN†, AND DAVID J. DEROSIER‡

W. M. Keck Institute for Cellular Visualization, Rosenstiel Basic Medical Sciences Research Center, Department of Biology, Brandeis University, Waltham, MA 02254

Communicated by Howard C. Berg, Harvard University, Cambridge, MA, June 11, 1999 (received for review April 3, 1999)

ABSTRACT **FliG, FliM, and FliN, key proteins for torque generation, are located in two rings. The first protein is in the M ring and the last two are in the C ring. The rotational symmetries of the C and M rings have been determined to be about 34 (this paper) and 26 (previous work), respectively. The mechanism proposed here depends on the symmetry mismatch between the rings: the C ring extends 34 levers, of which 26 can bind to the 26 equivalent sites on the M ring. The remaining 8 levers bind to proton–pore complexes (studs) to form 8 torque generators. Movement results from the swapping of stud-bound levers with M ring-bound levers. The model predicts that both the M and C rings rotate in the same direction but at different speeds.**

The bacterial flagellum [reviewed by Namba and Vorderviszt (1)], the organ of motility in *Salmonella typhimurium* and many other species of prokaryotes, is powered by a reversible rotary motor. The motor is embedded in the cell envelope, possesses up to eight torque-generating units (2, 3), and is powered by a H^+ gradient across the cytoplasmic membrane (4, 5). Each revolution consumes ≈1,000 H^+ (6) and requires ≈400 steps (7).

Initial observations (8, 9) of the cell-proximal end of the flagellum, the site of the motor, revealed an assembly, known as the basal-body complex, composed of several rings surrounding an axial structure. This axial structure extends from the cell to form the flagellar propeller, also known as the filament. Initially, there were four rings in basal-body complexes extracted from *S. typhimurium*. The L and P rings are associated with the lipopolysaccharide and peptidoglycan layers of the outer membrane, respectively, and are thought to serve as bushings. Two proteins (FlgH and FlgI) make up this structure (10). The S ring sits in the periplasm next to the inner membrane. The M ring crosses the cytoplasmic membrane and serves to transfer torque from the motor to the axial structures on the outside of the cell. A single protein, FliF, gives rise to both the M and S rings (11). Quantitative gel electrophoresis and autoradiography based on ^{35}S-radiolabeling of basal-body complex proteins (12) and scanning transmission electron microscopy mass measurements of purified basal-body complexes (13) reveal that there are 26 (± ≈2) copies of each of the proteins comprising the L, P, and MS rings. FliG, a protein important in torque generation, binds to FliF, producing a thickened M ring (14, 15). Throughout this paper, when we refer to the M ring, we mean this extended structure of FliG bound to FliF.

More recently, a fifth ring has been revealed in preparations of basal-body complexes extracted with less harsh isolation procedures (15–17). This ring is referred to as the C (cytoplasmic) ring and minimally appears to contain FliM and FliN (15), proteins that are also involved in motor function. The flagellar motor appears to have a 1:1 FliG/FliF stoichiometry (18), implying that there are ≈26 copies of FliG. Quantitative immunoblot analysis, however, indicates that there are 41 ± 10 copies of FliG, 35 ± 13 copies of FliM (19), and 111 ± 13 copies of FliN (20) associated with each wild-type basal body. It is not clear how to reconcile the differing estimates of FliG stoichiometry except to note that the methods are subject to different systematic errors. Other lines of evidence (21) suggest that the stoichiometry of FliN/FliM is more than 1:1. Given the errors in the estimates, the number of subunits of FliM, and hence the rotational symmetry of the C ring, are uncertain.

In the membrane surrounding the motor is a circle of studs, which are thought to contain MotA and MotB and to correspond to the independent torque generators described by Block and Berg (22) and Blair and Berg (2). Whereas Blair and Berg find at most eight torque generators, Khan *et al.* (3) find an average of 10 studs. The lack of correspondence between these numbers remains unexplained.

We report in this manuscript on the rotational symmetry of the C ring both in wild-type preparations and in preparations from a mutant involving a fusion of FliF to FliG. Based on these observations and those previously reported, we propose a new model for the mechanism of motor rotation.

MATERIALS AND METHODS

Specimen Preparation, Electron Microscopy, and Digitization. Hook/basal-body complexes were prepared from three different *S. typhimurium* strains. Although strain SJW880 exhibits the polyhook phenotype described by Patterson-Delafield *et al.* (23) and is nonmotile, its genetic background is otherwise wild-type for motor function. Strains SJW3821 and MYR1101 contain different in-frame deletions between the end of *fliF* and the beginning of *fliG*. These deletions generate fusion proteins that have lost differing amounts from the C terminus of FliF and the N terminus of FliG (18). The fusion protein from strain MYR1101 is essentially full length. We refer to this as the full-length fusion mutant. The fusion protein from strain SJW3821 has lost 10% of FliF (56 amino acids of 560) and 28% of FliG (94 amino acids of 331). We refer to this as the deletion-fusion mutant. Motors in both mutants rotate, although the motor from the deletion-fusion mutant does so poorly (18). The motor with the full-length fusion protein has a clockwise bias, whereas motors with the deletion-fusion protein have a counterclockwise bias.

Filaments make up ≈99% of the mass of a preparation of flagella, and their presence often obscures images of flagellar motors. Because filaments can be genetically removed without impairing motor function, we have chosen to work with such strains: strain SJW880 produces very few flagellar filaments because of the polyhook phenotype, whereas strains SJW3821 and MYR1101 have had filament production eliminated genetically. Strain SJW3821 was supplied by S. Yamaguchi (Izume

The publication costs of this article were defrayed in part by page charge payment. This article must therefore be hereby marked "*advertisement*" in accordance with 18 U.S.C. §1734 solely to indicate this fact.

PNAS is available online at www.pnas.org.

*Present address: Structural Biology Program, European Molecular Biology Laboratory, Heidelberg 69117, Germany.
†Present address: The Department of Biophysics, Boston University School of Medicine, Boston, MA 02118 and Department of Cell Biology, Harvard Medical School, Boston, MA 02254.
‡To whom reprint requests should be addressed.

Campus, Meiji Univ., Tokyo) and the other strains by R. Macnab (Yale Univ., New Haven, CT).

The preparation of hook–basal-body complexes from these strains followed procedures previously described (15) but with modifications. Cells were grown in eight 1-liter cultures, and at late-logarithmic stage (8–10 hours), the cells were pelleted at 4,000 × *g* for 20 min. The pellets were resuspended in 500 ml of ice-cold 0.5 M sucrose, 50 mM Tris·HCl (pH 8.0). The preparation was divided into two and kept on ice. Eight milliliters of 0.5 M EDTA (pH 8.0) was added to each of the two samples to bring the final concentration of EDTA to about 8 mM. The solutions were stirred for 30 min, after which 15 ml of lysozyme at 2 mg/ml was added. The incubation continued for 30–60 min on ice with stirring. Unlysed cells were removed by centrifugation at 4,000 × *g* for 20 min. The supernatant was adjusted to pH 11 by dropwise addition of 5 M NaOH and then centrifuged for 70 min at 90,000 × *g*. The pellets were resuspended in 30 ml of 100 mM KCl, 10% (wt/vol) sucrose, 0.1% (vol/vol) Triton X-100, and 10 mM Tris·HCl (pH 8.0). The resuspended preparations were centrifuged at 4,000 × *g* for 10 min to remove debris. The supernatants were then centrifuged at 120,000 g for 60 min, and the pellets were resuspended in 100 to 500 μl of 0.1% vol/vol Triton X-100, 5 mM EDTA, 10 mM Tris·HCl, pH 8.0. This basal-body preparation was then run on a Percoll (Bio-Rad) density gradient, and the Percoll beads were removed by gel filtration, by using an S-1000 (Bio-Rad) column as described by Khan *et al.* (16). The complexes are stable on ice for several weeks.

Frozen, hydrated samples were prepared in a cold room by placing 4 μl of a basal-body preparation on a copper grid covered by a perforated carbon film. The carbon films were prepared according to the procedure of Fukami and Adachi (24). The hole sizes varied considerably but were in the range of microns. After 30–60 sec, the excess fluid was blotted by using no. 40 filter paper (Whatman), and the grid was plunged into liquid nitrogen-cooled ethane, stored under liquid nitrogen, and transferred into a CM12 electron microscope (Philips Electronic Instruments, Mahwah, NJ) equipped with a model 651 anticontaminator and a model 626 cold stage (Gatan, Pleasanton, CA). Images were taken at ×60,000 on SO-163 film (Eastman Kodak) with a dose of about 10 e/Å^2 at ≈1 μm under focus. Images were digitized at 3.3 Å per pixel on an Eikonix (Bedford, MA) densitometer.

Data Analysis. All images of the hook–basal-body complexes were processed by using the single-particle methods in SPIDER (25).

Top views of the hook–basal-body complex were centered by using cross-correlation methods. A tight annular mask was used to eliminate most of the background area from each image. Each masked image was rotationally aligned to a reference image (one of the three top views) and averaged. In addition, each top view was rotationally aligned to itself, and the positions of local cross-correlation maxima were plotted as a function of rotation angle. Finally, Fourier transforms of these masked images were calculated, and the positions of rings of peaks in the transform were determined.

Alignment and averaging of side views of the hook–basal-body complex have been described previously (15, 26). C rings were boxed from each image and aligned. We subtracted the average C-ring image, which is a good approximation to the cylindrically averaged structure (26). The resulting densities were projected onto a line perpendicular to the flagellar axis, and a one-dimensional Fourier transform was computed. The power spectrum of this transform was calculated, and power spectra from all the aligned images were averaged.

Determination of the Rotational Symmetry of the C Ring. We determined the rotational symmetry of the C ring by analyzing the Fourier transforms of ring images. The theory for the diffraction from rings is similar to the theory for helical structures (27) because a ring of *n* subunits is a special case of a helix in which each successive subunit is rotated by 360°/*n* but is not translated axially. The transform of a helix is described in terms of layer lines each having a particular order *n*. In the transform of a ring, all of the layer lines superpose. Thus, the transform of a ring of *n* points is

$$F(R,\Psi) = \sum_{k=-\infty}^{\infty} J_{kn}(2\pi rR)e^{ikn\Psi} \qquad [1]$$

where R and Ψ are the cylindrical coordinates of the transform and r is the radius of the ring of points.

To illustrate the transforms of rings and our procedures for analyzing them, we constructed model images. We generated a series of projection images of a model C ring having 34-fold (see experimental data below) rotational symmetry (Fig. 1*A*). Each subunit in the model is a sphere.

The Fourier transform of a model ring of subunits (viewed from the top) consists of concentric rings (Fig. 1*B*). The innermost set of rings corresponds to the $k = 0$ or J_0 term of Eq. **1**; that is, to the low-resolution features that are cylindrically symmetric. The rings near the center of the transform tend to be the strongest, whereas those lying farther from the center are weaker. Before the rings from the cylindrically symmetric part fade out entirely, a second set of rings appears. These rings, which are usually stronger than the fading rings from the previous set, arise from the J_n and J_{-n} term; that is, from the division of the ring into subunits. The position of the first maximum (see ∗, Fig. 1*B*) provides a measure of *n*, the rotational symmetry of the structure.

In analyzing helical structures, one can estimate *n*, the order of a layer line, from the position of the first maxima, R_{peak}, on that layer line and r_0, the radius of the helical structure (27). One can

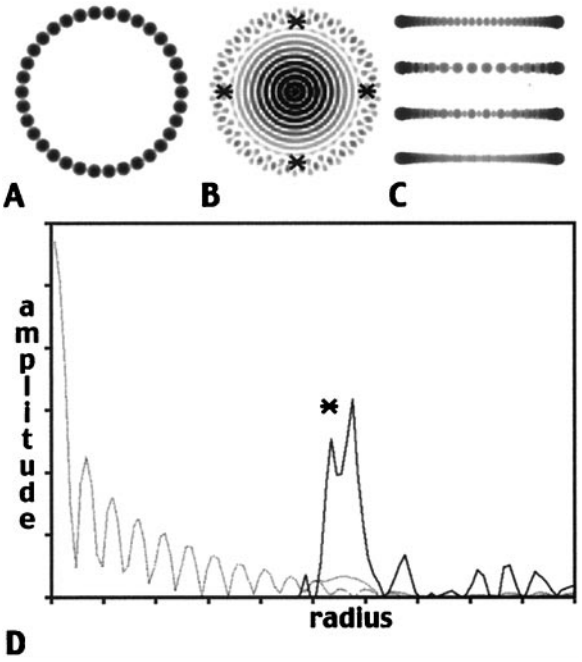

FIG. 1. Computer-generated models of a ring and their Fourier transforms. (*A*) Top view of a ring of 34 spherical subunits. (*B*) Fourier transform of *A*. The inner part of the transform consists of narrowly spaced, uniform rings of intensity. This pattern corresponds to the J_0 term of the transform. At the edge, a stronger, periodic ring appears, which corresponds to the J_{34} term of the transform (∗). (*C*) Side views of the ring. The upper three images correspond to side projections of the ring in *A* taken at different orientations. The bottom view is the average of a set of 100 side projections taken at different angles. Note that the periodicity seen in the first three is effectively lost in the averaging process. (*D*) Power spectra derived from the Fourier transforms of the side views. The dashed curves correspond to the average of the power spectra of the 100 side views taken at random orientations and to the power spectrum of the average of the 100 side views. The solid line is the difference of the two, which has been scaled up by a factor of 10. ∗ marks the start of the J_{34} term seen in *B*.

similarly estimate the rotational symmetry of the C ring. Because we expect the rotational order of the C ring to be large, we have chosen to use the following equation (28) to determine n.

$$2\pi r_0 R_{peak} = 1.03|n| + 1. \quad \textbf{[2]}$$

Eq. **2** has a simple explanation: $2\pi r_0$ is the circumference of the C ring, and R_{peak} is approximately the inverse of the spacing between subunits. Thus, the circumference divided by the spacing between subunits gives an estimate of the number of subunits, n.

In the Fourier transform (Fig. 1*B*) of the ring, the peak is found at a radius of 39 pixels. Because the dimension of the transform is 1,024, $R_{peak} = 39/1024 = 0.038$ reciprocal pixels, which is the radial position of the first peak in the second set of rings (see * in Fig. 1*B*). In the model, the radius of the ring is $r_0 = 151$ pixels. With these values for r_0 and R_{peak}, we can use Eq. **2** to compute n:

$$2\pi \times 0.038 \times 151 = 36.1 = 1.03|n|+1, \quad \textbf{[3]}$$

which gives an estimate of n of 34.

We can apply this procedure to the side views of our model ring. We show three side views of our model (top three images in Fig. 1*C*). Each image corresponds to a different angular orientation. We calculated 100 such side projections taken at random angles. An average of the 100 random side views is shown in the bottom image in Fig. 1*C*. We projected each of the 100 rings onto a horizontal line. We calculated the Fourier transforms of these projections and averaged their power spectra. We also calculated the power spectrum for the projection obtained from the averaged images of the ring. We computed the difference between the average of the power spectra and the power spectrum of projected average ring. Plots of the power spectra and their difference are shown in Fig. 1*D*. These spectra correspond to central sections of the Fourier transform of the top view (i.e., along a line through the center of the transform as shown in Fig. 1*B*). In the figure, we see a set of peaks near the origin corresponding to J_0 and at a radius of R_{peak} we find the peak corresponding to J_n. We can obtain an estimate of r_0 from the side images and an estimate of R_{peak} from the difference power spectrum. We can insert these into Eq. **2** to estimate n, as with the top views.

We can therefore estimate the rotational symmetry of the C ring by using either the three top views or the many side views of the C ring. These two estimates are independent, but they should and do agree.

RESULTS

Top Views. We found several *en face* views of the C ring as judged by the diameter of the image and by features such as the M ring, which can be discerned inside. Fig. 2 *A–C* present the three best *en face* views. The diameter of the C ring (≈450 Å) is the same as that observed in the side views. Images of both the top and side views appear serrated, indicating that subunit detail is visible in the C ring. Subunits are not clearly resolved everywhere, and a straightforward count of the number of subunits was not possible.

We unsuccessfully attempted to align and average the top views shown in Fig. 2 *A–C*. The average did not produce clear subunit detail around the entire circumference of the ring (data not shown). We were able to estimate the rotational symmetry, however, by rotationally aligning each image to itself and plotting the position of local cross-correlation peaks as a function of rotation angle (Fig. 2*F*). If the data were perfect, we should see n equally spaced peaks. Although these data are not perfect, the peaks from images in Fig. 2 *A–C* are nearly evenly spaced except that Fig. 2*A* has four gaps where peaks appear to be missing. Peak positions in Fig. 2 *A* and *C* are essentially in register, whereas those from Fig. 2*B* fall out of register as the angle moves away from 0°. For the plots from Fig. 2 *A* and *C*, we determine there are 34 peaks, whereas for that from Fig. 2*B* we obtain 33.

Images in Fig. 2 *B* and *C* appear to be the nearest to circular. When these are compared (Fig. 2 *B′* and *C′*), the diameters of the individual images differ (Fig. 2*D*): the image in Fig. 2*C* has a radius, r_0, of 225 Å, whereas the radius of the image in Fig. 2*B* is ≈4% smaller. The rings are not perfectly round, perhaps because of a slight tilt from the perfect *en face* view. The fact that the ring in Fig. 2*B* appears smaller is consistent with its having fewer subunits.

Before turning to the analysis of side views, we determined the radius, R_{peak}, at which the peak corresponding to J_n occurs (in the same way as was done in the model image and transform in Fig.

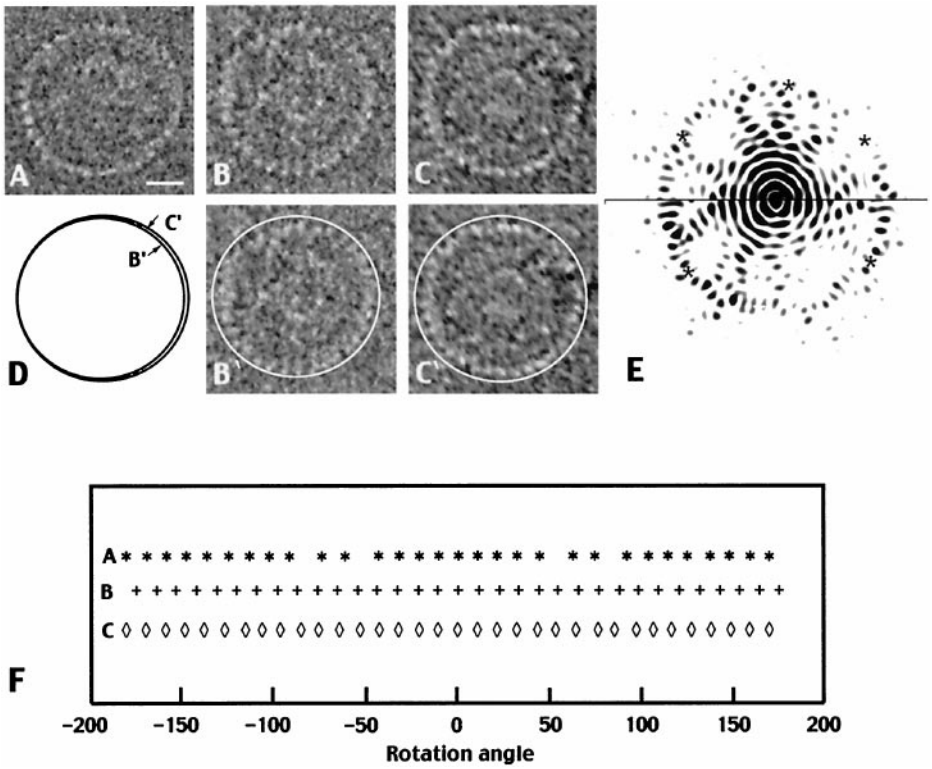

FIG. 2. Gallery of basal-body images. (*A–C*) The three good top views. *B′* and *C′* are copies of *B* and *C* with ellipsoids drawn to correspond to the circumference of the rings. (*D*) A comparison of the two ellipsoids from *B′* and *C′* showing that the ring in *B* is smaller than that in *C*. (*E*) Fourier transforms of two top views spliced together (the top half corresponds to the ring in *A*; the bottom half corresponds to the ring in *B*). * marks the positions of the J_{34} and J_{33} terms. The peaks in both transforms occur at a radius of 1/39 $Å^{-1}$. (*F*) A plot of local cross-correlation peaks vs. rotation angle for the three top views shown in *A–C*. The peaks provide a measure of the number of subunits in each C ring. There should be one peak for each subunit. There are four gaps in the plot for the ring in *A*, which presumably correspond to four missing peaks. Allowing for these missing peaks, we determine that $n = 34$ count for the rings in *A* and *C*, and $n = 33$ for the ring in *B*. (Bar = 100 Å in *A*.)

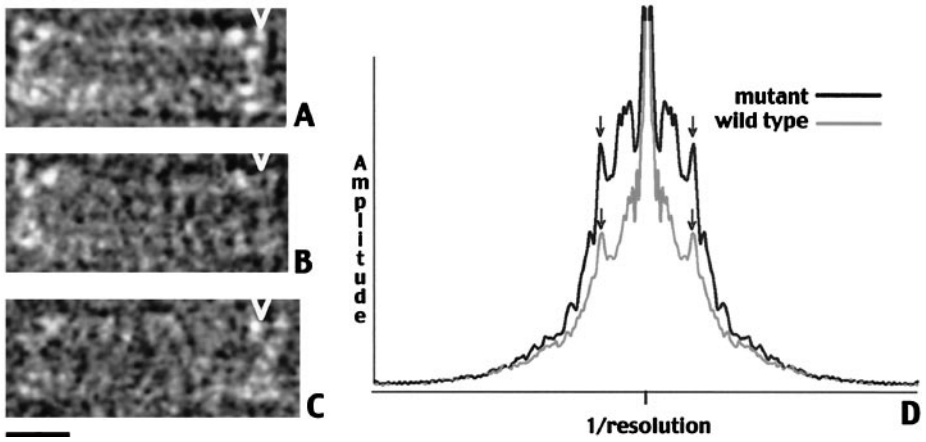

FIG. 3. (*A–C*) Three side views of the C ring. Note that the rings are of different diameter. The left sides are aligned, and one of the units in *A* is marked with an arrowhead. The arrowhead is repeated at the same spatial position in *B* and *C* to make the difference in diameter clearer. (Bar = 100 Å.) (*D*) Fourier transforms of side views. The side views are projected onto a line perpendicular to the axis. The projection of the average of these views (Fig. 4 *A* or *B*) is subtracted. The amplitude distribution of the Fourier transforms of these differences projections are averaged. The two curves display the amplitudes corresponding to the wild-type and to the deletion-fusion mutant. There are peaks at a radius of 1/39 $Å^{-1}$ (see arrows), the same position as the peaks seen in Fig. 2*E*.

1 *A* and *B*). This radius should be the same as that seen in transforms of side views. Fig. 2*E* shows half-transforms of Fig. 2 *B* and *C* positioned so that they oppose each other. Although these images and their Fourier transforms are noisy, a ring of diffraction maxima occurs in each transform. The average positions of these maxima have been marked with asterisks in each half transform. The two half-circles have essentially identical radii: R_{peak} = 1/39 $Å^{-1}$, which indicates that the subunit spacings in the two rings are the essentially the same. The measurements of R_{peak} of the transform and the radius r_0 of the ring should provide an estimate of n by using Eq. **2**. The errors in measuring the radius R_{peak} are sufficiently large that we cannot be sure that the values of R_{peak} for the two transforms are the same. If the two values of R_{peak} for the two transforms are indeed the same, then the ring in Fig. 2*C* would have about $n = 2\pi \times 225/39 = 34$ subunits, whereas the ring in Fig. 2*B* would contain 1 fewer subunit because its diameter is 4% smaller.

Side Views. Fig. 3 *A–C* show three typical side views. Note that the diameters of the C rings seen in these side views are not the same. The variation could arise from flattening or from a variation in the number of subunits. The diameter in Fig. 3*A* is 3% smaller than that in Fig. 3*B*, whereas that in Fig. 3*C* is ≈3% larger. We began by aligning and averaging 90 equal-sized side views of the basal-body complexes. Fig. 4*A* shows the average. We then selected just the C-ring portion and projected it as was done for the model in Fig. 1. We subtracted the projection of the averaged C-ring image from each of 90 projections to obtain 90 difference projections. We calculated and averaged the power spectrum of the 90 difference projections. The result (Fig. 3*D*) contains a peak at a radius R = 1/39 $Å^{-1}$, the same radius as that found for the top views. A variation in the number of subunits in a ring has essentially no effect on the spacing R_{peak}. From the radius of the C ring (225 Å) and the radius of the peak (1/39 $Å^{-1}$), we again get an estimate of n = 34. The variation of 3% in diameter between the C rings in Fig. 3 *A–C* corresponds to a change of one subunit in n.

Analysis of C Rings from Hook–Basal-Body Complexes Containing FliF–FliG Fusion Proteins. Fig. 4 *B* and *C* show the results of aligning and averaging images of basal-body complexes from the deletion-fusion mutant and the full-length fusion mutant, respectively. The images were aligned by using their C rings. The images of C rings from the wild-type strain (Fig. 4*A*) and the full-length fusion mutant (Fig. 4*C*) have the same diameter and lie in the same position below the M ring, whereas the image from the deletion-fusion mutant (Fig. 4*B*) is narrower and overlaps the M ring. The diameters of the M and S rings, however, appear to be the same in all three averages (Fig. 4 *A–C*).

The 63 images of C rings in basal bodies from the deletion-fusion mutant were processed as described above. The trace of the averaged one-dimensional power spectrum is shown in Fig. 3*D*. There is a peak at the same position (R_{peak} = 1/39 Å) as that found in the spectrum corresponding to C rings from basal bodies of the wild-type strain. This correspondence means that the spacing between subunits in the C ring is the same in basal bodies derived from the wild-type and the deletion-fusion mutant. However, because the radius of the C ring in the mutant strain is smaller than that in the wild type (205 Å vs. 225 Å), there are fewer subunits in the former. From Eq. 2, we obtain an estimate for n of 31 for the C ring of the deletion-fusion mutant. We had too few intact C rings in images of basal bodies from the full-length fusion mutant to process them in this manner.

DISCUSSION

Rotational Symmetry of Wild-Type C-Ring Complexes. Both top and side views give rise to an estimated number of C-ring subunits of about 34, consistent with values reported previously (19). We also obtained evidence that this number can vary in wild-type motors by one subunit and in motors from the deletion-fusion mutant by three subunits. The mutant provides a particularly compelling case for the number 31 because it derives from a large number of images having an obvious 10% change in radius

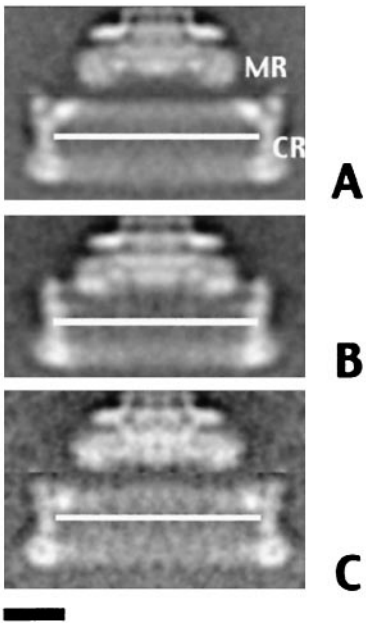

FIG. 4. Averaged images of basal bodies. (*A*) Average of wild-type basal bodies embedded in vitreous ice. The M and C rings are labeled MR and CR, respectively. (*B*) Average of basal bodies from the deletion-fusion mutant. (*C*) Average of basal bodies from the full-length fusion mutant. The bar in each image is drawn to the same length to demonstrate the change in the diameter of the C ring. (Bar = 100 Å.)

of the C ring yet having the same subunit spacing as that found in the wild-type C ring. The fact that the mutational changes are in FliF and FliG, components of the M ring, suggests that the M ring, at least in part, dictates the symmetry of the C ring. We suppose that in the deletion-fusion mutant, the radius at which the C ring attaches to the M ring is decreased. This reduction in radius reduces the circumference of the C ring, and hence the number of C-ring subunits that can be accommodated is fewer, given that the spacing between C-ring subunits is unchanged.

The Relationship Between the C and M Rings. We might expect that a well defined cellular structure like the C ring has a fixed stoichiometry of subunits. The M ring, however, presents only 26 equivalent sites (12, 13) to which the C ring can attach. We argue, therefore, that the number of interactions between the M and C rings is the same for motors in which the rotational symmetry of the C ring is 31, 33, or 34. If, on average, the wild-type C ring has 34 subunits, there will be $34 - 26 = 8$ positions on the C ring for which there is no corresponding subunit of the M ring. We call these eight positions symmetry-mismatch positions.

A Model for the Motor. We have built a simple model (Fig. 5) in which torque is generated at the symmetry mismatch positions. The model is based on our observations of the structure and its numerology. It has no underpinnings in the energetics of motor function. In our model, the C-ring subunits extend 34 levers, of which 26 can attach to 26 equivalent sites on the extended M ring. There is evidence that FliG and FliM interact with each other (29–31). The reason for postulating a lever is that in wild-type motors, there is no obvious bridge of density between the C ring and the M ring. Thus, the actual connections between the two rings must be relatively low-mass extensions, which are lost on image averaging. We postulate that the levers are part of FliM, although there is no evidence for this. We further postulate that eight MotA–MotB complexes (studs) attach to the eight free levers. There is evidence that MotA and MotB interact with FliG and FliM (29–34). Protons delivered by the MotA–MotB complex are coupled to the swapping of a stud-attached lever with an M ring-attached lever. It is this swapping that generates the torque.

In Fig. 5*A*, we display a contoured plot of the averaged image seen in Fig. 4*A*, extended to include all of the rings and part of the hook. We have added thin levers connecting the C ring to the M ring. We have also added an element corresponding to the MotA–MotB stud, which we have anchored on the peptidoglycan layer located at the position of the P ring (35–37). The inner and outer membranes (located at the position of the M and L rings, respectively) are not shown. We are interested in the portion of the motor contained inside the box. We represent the M and C rings as lines with elastic levers extending from them, and we have taken liberties with the geometry to simplify the cartoon. In Fig. 5*B*, the C ring extends five levers up toward the four lever-binding sites on the M ring. Four of the C ring levers bind to these four sites on the M ring. The fifth lever at the symmetry-mismatch position forms a complex with the MotA–MotB stud, shown with its connection to the peptidoglycan layer. This attachment reminds us that the studs are part of the stator, or fixed part of the motor. The stud–C ring lever complex swings (perhaps by Brownian motion), extending to the left where it attaches to the adjacent C ring–M ring lever complex. Thus, we have a complex consisting of a stud (Mot A and MotB), two levers (FliM), and FliG, all of which are known to interact. We assume torque is generated by extension of the elastic elements in the lever–stud complex. Thus, both the C ring and the M ring begin to move (Fig. 5 *C* and *D*). The stud now effects the swapping of one C ring lever for the other (Fig. 5 *D* and *E*). After the lever swap, the stud will dissociate, taking with it the lever previously bound to the M ring. Again, torque is generated on dissociation because one of the restraints on the M ring and the C ring is removed. Both the M and C rings will move (Fig. 5 *E* and *F*). Note that during lever swapping, the two rings remain bound to one another and to the studs. Thus, the motor would be processive.

At the end of the cycle, both the M ring and C ring move, each by one asymmetric unit. Because the two rings have different numbers of asymmetric units (26 vs. 34), the two rings move by different angular amounts. The M ring takes 1/26th of a revolution and the C ring 1/34th of a revolution. This means that the M and C rings move relative to each other and to the stud, which is anchored to the cell envelope. An interesting consequence of this

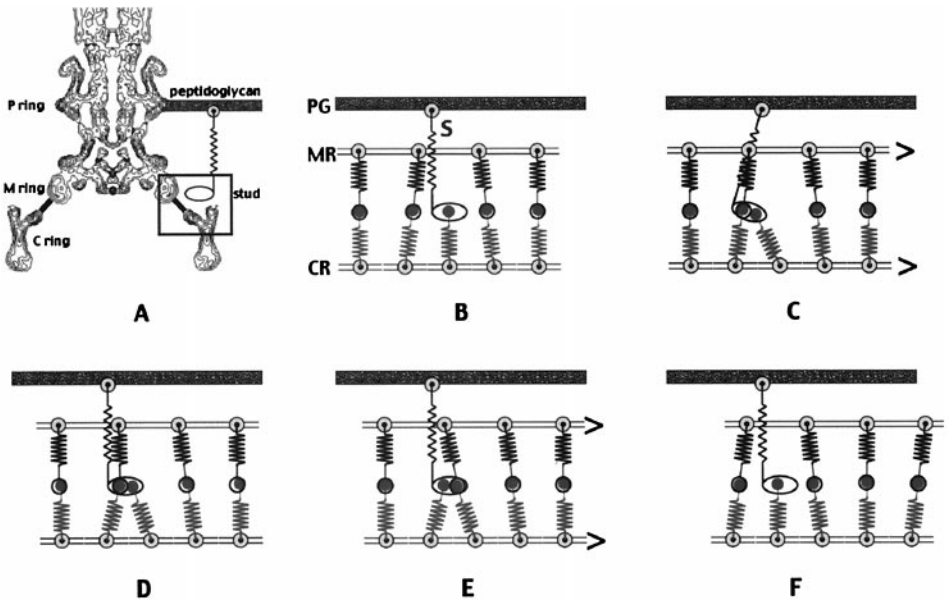

FIG. 5. Schematic of the model for the mechanism of motor rotation. (*A*) A contour plot of the density of the averaged image in Fig. 4*A*, except that the L and P rings and part of the hook are included. The stud and its connection to the peptidoglycan layer are shown in cartoon form. The stud is not attached to the C or M ring here, but it is in *B*. The bar connecting the C ring and the M ring is intended to represent the C ring levers and their binding sites on the M ring. The zig-zag lines here and in Fig. 3*F* depict possible elastic elements. The box indicates the part of the motor shown in cartoon form in *B–F*. (*B*) The model represents a short segment of the full motor. It shows five of the C ring (CR) subunits, four of the M (MR) ring subunits, and one stud (MotA–MotB complex). The difference in the number of subunits in the M and C rings in the model represents the differences in the number of subunits in these rings in the basal body. In particular, not all 34 levers from the C ring can mate with the bonding sites on the M ring, which has only 26 sites. The extra levers in our model form a complex with the MotA–MotB stud(s). In the model, we have shown only one extra lever, which is in a complex with a stud. We assume that all of the forces from the elastic elements are initially in balance. (*C*) The stud and unpaired C ring lever move, perhaps by Brownian motion, to the left and bind to the M ring–lever complex. On binding, the elastic elements generate a force, and the M and C rings move. (*D*) Motion stops when the forces are again balanced. (*E*) The unpaired lever from the C ring is now swapped so that it is bound to the M ring, and the stud and its new partner in the C ring are freed from the complex. Force is generated, and the M and C rings again move. (*F*) When the motion stops, the M ring and C ring have each moved by one subunit, and hence by different angles. The M ring has undergone 1/26 of a revolution, whereas the C ring has only undergone 1/34 of a revolution.

model is that if the filament of a cell is tethered so that cell body rotates, the M ring will be fixed but the C ring will rotate with a rate that is 8/34 the rotation rate of the cell body.

The model accounts for the eight independent torque generators, because there are eight symmetry-mismatch positions at which torque can be generated. In our model, if there were only one stud, there would be only one site at which swapping is taking place. The single stud–lever complex would generate one unit of torque. A second stud could work independently of the first, because it has its own site. It would generate an additional unit of torque. Only eight studs can produce torque because there are only eight sites with a free lever. Thus, one should only see eight incremental increases in torque regardless of the number of studs or MotA–MotB complexes found at each motor. This could resolve the puzzle of why Khan *et al.* (3) find an average of 10 studs but Blair and Berg (2) find only 8 torque generators. The model also accounts for the ability of the motor to rotate despite the remarkable change in structure in the deletion-fusion mutant. The reason is that the sites of attachment between the two rings are also the sites of torque generation and that these attachments are retained in the mutant, albeit moved to a smaller radius. The motor can work equally well backwards or forwards simply by switching the direction in which swapping proceeds. We have not postulated a mechanism for the determination of direction, but it may be that some feature on the C ring can obstruct the swinging of the lever arms in one direction. Such a steric block would have to apply to all eight free lever arms and would have to be switchable in a cooperative fashion to reverse motor rotation.

The Number of Torque-Generating Events per Revolution in the Model. As proposed in Fig. 5, there are two torque-generating events per cycle. The first occurs when the free lever arm and stud attach to one of the occupied sites on the M ring (Fig. 5*C*), and the second occurs when, after swapping lever arms, the stud and swapped lever arm detach (Fig. 5*E*). If there are 26 steps per revolution of the M ring, then there are $26 \times 2 = 52$ torque-generating events per revolution per torque generator. If there are eight torque generators then, when all are operational, there would be $52 \times 8 = 416$ torque-generating events per revolution. These would be seen as discrete events if the two different kinds of torque generating events have about the same time constants. Our model is consistent with the 400 steps detected by Samuel and Berg (7).

Current measurements estimate that 1,000 protons are consumed per revolution. If taken at face value, it would mean that several protons are used per torque-generating event. The proton or protons could be used at any step; for example, the protons could be used in the binding or release reaction and/or in the swapping of lever arms. There is no data to suggest one possibility over another.

We have proposed a new model for the mechanism of motor rotation. It is based on structural observations, but it can account both for the observed eight torque generators and for the 400 steps per revolution. It makes testable predictions. First, when a cell is tethered by one of its filaments, the C ring will rotate but at a rate that is 8/34 the rate of cell body rotation. Second, the number of torque generators will decrease with a decrease in the number of subunits in the C ring.

We thank Bob Macnab and Howard Berg for discussions, and we gratefully acknowledge the help of Carol Palmer and Andy Brilliant in preparing this manuscript and figures. This project was supported by funds from National Institute of General Medical Sciences (R01 GM35433 and T32 GM07596) and from a grant from the W. M. Keck Foundation.

1. Namba, K. & Vonderviszt, F. (1997) *Q. Rev. Biophys.* **30,** 1–65.
2. Blair, D. F. & Berg, H. C. (1988) *Science* **242,** 1678–1681.
3. Khan, S., Dapice, M. & Reese, T. S. (1988) *J. Mol. Biol.* **202,** 575–584.
4. Manson, M. D., Tedesco, P., Berg, H. C., Harold, F. M. & Van der Drift, C. (1977) *Proc. Natl. Acad. Sci. USA* **74,** 3060–3064.
5. Matsuura, S., Shioi, J. & Imae, Y. (1977) *FEBS Lett.* **82,** 187–190.
6. Meister, M., Lowe, G. & Berg, H. C. (1987) *Cell* **49,** 643–650.
7. Samuel, A. D. & Berg, H. C. (1995) *Proc. Natl. Acad. Sci. USA* **92,** 3502–3506.
8. DePamphilis, M. L. & Adler, J. (1971) *J. Bacteriol.* **105,** 384–395.
9. Cohen-Bazire, G. & London, J. (1967) *J. Bacteriol.* **94,** 458–465.
10. Jones, C. J., Homma, M. & Macnab, R. M. (1987) *J. Bacteriol.* **169,** 1489–1492.
11. Ueno, T., Oosawa, K. & Aizawa, S. (1994) *J. Mol. Biol.* **236,** 546–555.
12. Jones, C. J., Macnab, R. M., Okino, H. & Aizawa, S. (1990) *J. Mol. Biol.* **212,** 377–387.
13. Sosinsky, G. E., Francis, N. R., DeRosier, D. J., Wall, J. S., Simon, M. N. & Hainfeld, J. (1992) *Proc. Natl. Acad. Sci. USA* **89,** 4801–4805.
14. Zhao, R., Schuster, S. C. & Khan, S. (1995) *J. Mol. Biol.* **251,** 400–412.
15. Francis, N. R., Sosinsky, G. E., Thomas, D. & DeRosier, D. J. (1994) *J. Mol. Biol.* **235,** 1261–1270.
16. Khan, I. H., Reese, T. S. & Khan, S. (1992) *Proc. Natl. Acad. Sci. USA* **89,** 5956–5960.
17. Schuster, S. C. & Baeuerlein, E. (1992) *J. Bacteriol.* **174,** 263–268.
18. Francis, N. R., Irikura, V. M., Yamaguchi, S., DeRosier, D. J. & Macnab, R. M. (1992) *Proc. Natl. Acad. Sci. USA* **89,** 6304–6308.
19. Zhao, R., Amsler, C. D., Matsumura, P. & Khan, S. (1996) *J. Bacteriol.* **178,** 258–265.
20. Zhao, R., Pathak, N., Jaffe, H., Reese, T. S. & Khan, S. (1996) *J. Mol. Biol.* **261,** 195–208.
21. Kihara, M., Francis, N. R., DeRosier, D. J. & Macnab, R. M. (1996) *J. Bacteriol.* **178,** 4582–4589.
22. Block, S. M. & Berg, H. C. (1984) *Nature (London)* **309,** 470–472.
23. Patterson-Delafield, J., Martinez, R. J., Stocker, B. A. D. & Yamaguchi, S. (1973) *Arch. Mikrobiol.* **90,** 107–120.
24. Fukami, A. & Adachi, K. (1964) *J. Electron Microsc.* **13,** 26–27.
25. Frank, J., Radermacher, M., Penczek, P., Zhu, J., Li, Y., Ladjadj, M. & Leith, A. (1996) *J. Struct. Biol.* **116,** 190–199.
26. Stallmeyer, M. J., Aizawa, S., Macnab, R. M. & DeRosier, D. J. (1989) *J. Mol. Biol.* **205,** 519–528.
27. Klug, A., Crick, F. H. C. & Wyckoff, H. W. (1958) *Acta Crystallogr.* **11,** 199–213.
28. Unwin, N. (1993) *J. Mol. Biol.* **229,** 1101–1124.
29. Marykwas, D. & Berg, H. C. (1996) *J. Bacteriol.* **178,** 1289–1294.
30. Marykwas, D. L., Schmidt, S. A. & Berg, H. C. (1996) *J. Mol. Biol.* **256,** 564–575.
31. Tang, H., Braun, T. F. & Blair, D. F. (1996) *J. Mol. Biol.* **261,** 209–221.
32. Garza, A. G., Harris-Haller, L. W., Stoebner, R. A. & Manson, M. D. (1995) *Proc. Natl. Acad. Sci. USA* **92,** 1970–1974.
33. Garza, A. G., Bronstein, P. A., Valdez, P. A., Harris-Haller, L. W. & Manson, M. D. (1996) *J. Bacteriol.* **178,** 6116–6122.
34. Garza, A. G., Biran, R., Wohlschlegel, J. A. & Manson, M. D. (1996) *J. Mol. Biol.* **258,** 270–285.
35. DeMot, R. & Vanderleyden, J. (1994) *Mol. Microbiol.* **12,** 333–334.
36. Chun, S. Y. & Parkinson, J. S. (1988) *Science* **15,** 276–278.
37. Muramoto, K. & Macnab, R. M. (1998) *Mol. Microbiol.* **29,** 1191–1202.